ACS Chemical Neuroscience
Cite This: ACS Chem. Neurosci. 2017, 8, 2152-2158
Letter
pubs.acs.org/chemneuro

Finke–Watzky Two-Step Nucleation–Autocatalysis Model of S100A9 Amyloid Formation: Protein Misfolding as "Nucleation" Event

Igor A. Iashchishyn,[†,‡] Darius Sulskis,[†,§] Mai Nguyen Ngoc,[§] Vytautas Smirnovas,[§] and Ludmilla A. Morozova-Roche*[,†]

[†]Department of Medical Biochemistry and Biophysics, Umeå University, SE-901 87 Umeå, Sweden
[‡]Department of General Chemistry, Sumy State University, 40007 Sumy, Ukraine
[§]Department of Biothermodynamics and Drug Design, Institute of Biotechnology, Vilnius University, LT-10257 Vilnius, Lithuania

Supporting Information

ABSTRACT: Quantitative kinetic analysis is critical for understanding amyloid mechanisms. Here we demonstrate the application of generic Finke–Watzky (F-W) two-step nucleation–autocatalytic growth model to the concentration-dependent amyloid kinetics of proinflammatory α-helical S100A9 protein at pH 7.4 and at 37 and 42 °C. The model is based on two pseudoelementary reaction steps applied without further analytical constraints, and its treatment of S100A9 amyloid self-assembly demonstrates that initial misfolding and β-sheet formation, defined as "nucleation" step, spontaneously takes place within individual S100A9 molecules at higher rate than the subsequent fibrillar growth. The latter, described as an autocatalytic process, will proceed if misfolded amyloid-prone S100A9 is populated on a macroscopic time scale. Short lengths of S100A9 fibrils are consistent with the F-W model. The analysis of fibrillar length distribution by the Beker–Döring model demonstrates independently that such distribution is solely determined by slow fibril growth and there is no fragmentation or secondary pathways decreasing fibrillar length.

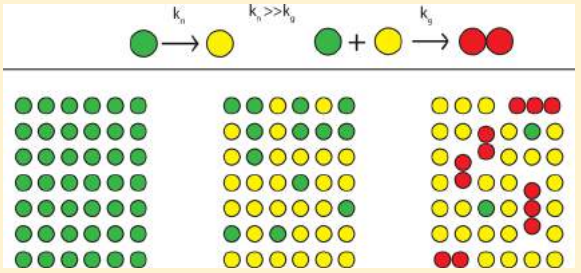

KEYWORDS: *Amyloid, autocatalysis, Finke–Watzky model, growth, kinetics, nucleation, S100A9*

Spontaneous amyloid self-assembly is a ubiquitous process associated with numerous human diseases, including Alzheimer's and Parkinson's diseases, type II diabetes, and others. Protein amyloid self-assembly in vitro is widely used in biotechnological applications. Remarkably, various structurally unrelated polypeptides, including natively unfolded proteins (such as α-synuclein), peptides (Aβ), as well as proteins containing α-helical (S100A9, apomyoglobin, cytochrome *c*), β-sheet (β-2-microglobulin) structures or combination of both (lysozyme, α-lactalbumin) are all able to self-assemble into amyloid fibrils containing cross-β-sheet. The mechanisms and kinetic models describing this fascinating process are in the focus of numerous research. To date there is no a single kinetic model which can describe the self-assembly of all known amyloidogenic proteins.[1] Nucleation was shown to be a critical step in amyloid formation.[1] In addition, the secondary nucleation mechanisms were identified to describe the amyloid growth.[2−4] Here we demonstrate the application of generic Finke–Watzky (F-W) two-step nucleation–autocatalytic growth model[5] to the concentration-dependent amyloid kinetics of α-helical protein S100A9. This model is based on two pseudoelementary reaction steps of nucleation and autocatalysis; the latter is considered as an underlying mechanism for fibrillar growth without any additional assumptions or constraints on the nuclei size and fibril propagation mechanisms such as secondary pathways. This generic model quantitatively described a wide variety of natural growth phenomena including inorganic nanocluster formation as well as some amyloid assemblies.[5,6]

S100A9, also known as migration inhibitory factor-related protein 14 (MRP14) or calgranulin B, is a multifunctional cytokine playing diverse roles in the inflammatory signaling pathways and its increased expression was reported in many ailments associated with inflammatory processes, including neurodegeneration and specifically Alzheimers disease,[7,8] traumatic brain injury,[9] cerebral ischemia,[10] malaria,[11] cardiovascular disease[12] and obesity.[13] The abundance of S100A9 mRNA was also found in various mammalian tissues including the central nervous system during aging, and a novel mechanism of the age-associated inflammation sustained by S100A9 was suggested.[14] By contrast to other proinflammatory cytokines, S100A9 is highly amyloidogenic and able to self-assemble into amyloids both in vitro and in vivo, which may lead to the loss of its signaling functions and acquiring amyloid cytotoxicity, exceeding toxicity of Aβ peptide manifested in Alzheimer's disease.[7] Therefore, the rising S100A9 level during inflammation may lead to its amyloid formation and deposition as we have shown in Alzheimer's disease,[7] aging prostate,[15] and

Received: July 5, 2017
Accepted: July 31, 2017
Published: July 31, 2017

DOI: 10.1021/acschemneuro.7b00251
ACS Chem. Neurosci. 2017, 8, 2152–2158

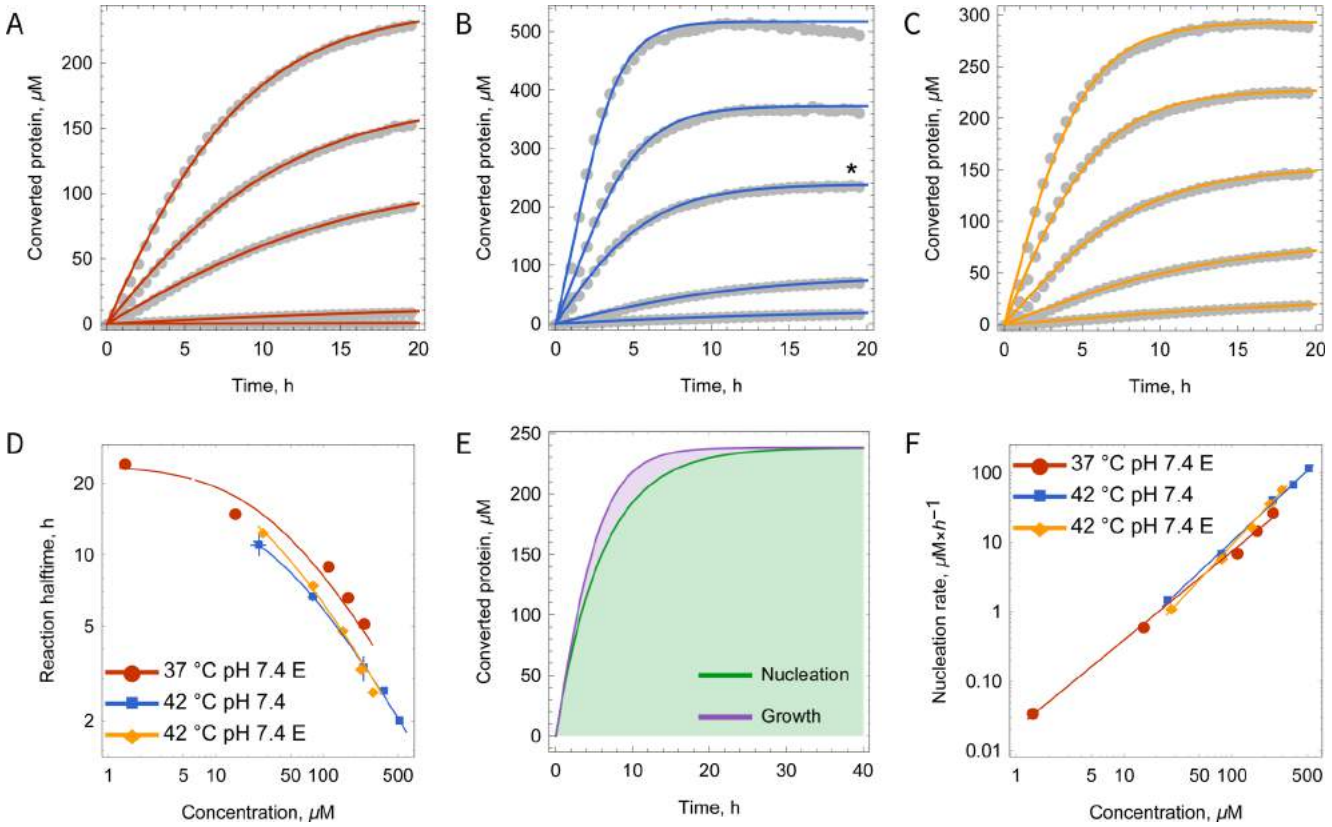

Figure 1. Application of the F-W two-step nucleation-autocatalysis model for the analysis of S100A9 amyloid formation kinetics. Amyloid formation kinetics with different initial concentrations of S100A9 monitored by ThT binding assay in PBS under the following conditions: (A) 37 °C, pH 7.4, 1 mM EDTA, (B) 42 °C, pH 7.4, and (C) 42 °C, pH 7.4, 1 mM EDTA. The experimental points are presented in gray in all figures; fitting curves are shown by red in (A), blue in (B), and yellow in (C). Concentration of S100A9 amyloids reactive with ThT is plotted along *y*-axis. (D) Half-time of amyloid formation (*y*-axis) plotted versus concentration of S100A9 amyloids (*x*-axis) for the conditions shown above in (A−C) and by the same color coding. Both *x*- and *y*-axes are presented in logarithmic scale. In the legend, EDTA is denoted as E. (E) Representative deconvolution of the kinetics of S100A9 amyloid formation presented in (B) and marked by an asterisk (*) into the contributions from nucleation (green) and growth (purple) reactions. (F) Nucleation rates ($k_n c$, *y*-axis) plotted versus concentration of S100A9 amyloids (*x*-axis) for the amyloid kinetics shown in (A)−(C). Both *x*- and *y*-axes are presented in logarithmic scale. In the legend, EDTA is denoted as E.

also in cell model for protein amyloid aggregation.[16] Moreover, the cerebrospinal fluid levels of S100A9 and Aβ match each other in Alzheimer's disease, vascular dementia and mild cognitive impairment,[17] suggesting involvement of S100A9 together with Aβ in the amyloid−neuroinflammatory cascade in these ailments. Importantly, S100A9 knockdown attenuated memory impairment and reduced amyloid plaque burden in an Alzheimer's disease mouse model,[18] further emphasizing the role of S100A9 in the amyloid cascade and indicating also that S100A9 can be a prospective therapeutic target in Alzheimer's treatment.

Therefore, here we shed further light on S100A9 amyloid formation process and showed that in the absence of stabilizing effect of calcium S100A9 amyloid self-assembly can spontaneously take place in a concentration-dependent manner under physiological pH 7.4 and 37/42 °C. The process of S100A9 amyloid conversion and assembly is well described by the generic F-W two-step model including nucleation and autocatalytic growth steps, while the contribution of amyloid dissociation is assessed by measuring the distribution of fibrillar lengths.

RESULTS AND DISCUSSION

The kinetics of S100A9 amyloid formation were monitored by thioflavin T (ThT) fluorescence assay under physiological pH 7.4 and at 37 or 42 °C, without agitations (Figure 1A−C). We have selected 42 °C as one of the temperatures for aggregation assays since it is close to physiological range, but enhances the rates and yield of S100A9 amyloid formation (Figure 1A).

Since S100A9 is a calcium-binding protein, in the control experiment, 1 mM $CaCl_2$ was added to S100A9 solution and it was incubated for 72 h. During this time, ThT fluorescence intensity remained close to the background level and amyloid fibrils were not observed by AFM imaging. Significant stabilization of S100A9 structure by calcium-binding in a wide range of pH was observed upon its thermal unfolding monitored by differential scanning fluorimetry in the presence of ANS (Figure S1), which is consistent with the calcium stabilizing effect reported previously.[19] This may lead to inhibition of S100A9 misfolding and amyloid assembly as we observed here. Moreover, calcium-binding promotes dimerization of S100A9,[7,20] which may hinder further its amyloid formation. Therefore, S100A9 amyloid formation was studied without addition of calcium or in the presence of 1 mM EDTA (Figure 1A−C). The amyloid growth proceeded without noticeable lag-phase and led to significant increase of ThT signal, which reached the plateau or stationary levels for all studied protein concentrations.

All kinetic curves (Figure 1A−C) were well fitted by the F-W two-step model of nucleation and autocatalytic growth,[5] which

DOI: 10.1021/acschemneuro.7b00251
ACS Chem. Neurosci. 2017, 8, 2152−2158

was applied previously to describe a broad range of nanoscale kinetic processes, including amyloid aggregations of 14 disease-related proteins.[6] The model involves two generic steps of the nucleation with rate constant k_n and the autocatalytic growth with rate constant k_g, in which nuclei play the role of autocatalysts for further amyloid conversion.

Our next step involved the analysis of the half-time of amyloid conversion plotted versus the concentration of converted amyloids (Figure 1D). Here the half-time corresponds to time point, when ThT fluorescence intensity reaches 50% plateau level in the kinetic curves (Figure 1A–C), and the concentration of amyloids (component B in eq 1) was determined from the pellet centrifuged after the completion of amyloid incubation as described in Methods. The experimental data points were very well fitted by using eq 4 (Figure 1D), confirming the validity of the selected F-W model.

It is interesting to note that all three dependences in Figure 1D are not linear as it would be in the case if the amyloid formation process was governed by the nucleation-dependent polymerization in accord with Oosawa's model and their negative slopes would then provide the estimates of the critical nucleus sizes.[21] Since our experimental and fitted dependences of the amyloid conversion half-times shown in Figure 1D decrease more steeply with increasing amyloid concentration than the linear functions, this indicates that there are two reactions—amyloid nucleation and amyloid growth and their contributions in the overall amyloid accumulation is demonstrated in Figure 1E.

The nucleation rates plotted versus the amyloid concentrations for all three separate conditions of S100A9 amyloid self-assembly at pH 7.4 (Figure 1A–C) are shown in Figure 1F and are characterized by almost similar slopes. The critical nucleus sizes calculated from these slopes according to eq 5 are all very similar and smaller than unity, indicating that the formation of amyloid β-sheet takes place within a single protein molecule and encompasses its most susceptible to amyloid conversion region. The amyloid propensity profile of S100A9 calculated previously[15] suggests that this part may include the polypeptide sequence corresponding to α-helix and adjusted loop in the N-terminal EF-hand and would be strongly modulated by calcium-binding as indeed this was observed in our amyloid formation experiments described above.

Thus, the F-W two-step model enables us to achieve the deconvolution of amyloid nucleation and growth steps, which is the central theme in the research focused on amyloid phenomenon. The concentration dependences of the nucleation k_n and growth k_g rate constants are presented in Figure 2. The left column, corresponding to the nucleation rate constants k_n at all three selected conditions at pH 7.4, shows that in all cases they increase linearly with increasing concentrations of amyloid converted protein. The nucleation rate constants k_n determined at 42 °C are slightly higher compared to those calculated at 37 °C (Figure 2). The growth rate constants k_g, corresponding to protein association into fibrils, remain constant, except the rate determined at lowest protein concentration in the presence of EDTA. They are also lower than corresponding nucleation rate constants k_n by an order of magnitude. This indicates that the nucleation dominates over amyloid growth in S100A9 amyloid formation at pH 7.4 and in the absence of calcium as demonstrated in Figure 1E. Even though the structure of S100A9 is significantly destabilized in the absence of calcium or at low calcium concentrations such as those found in vivo, it remains folded at both temperatures

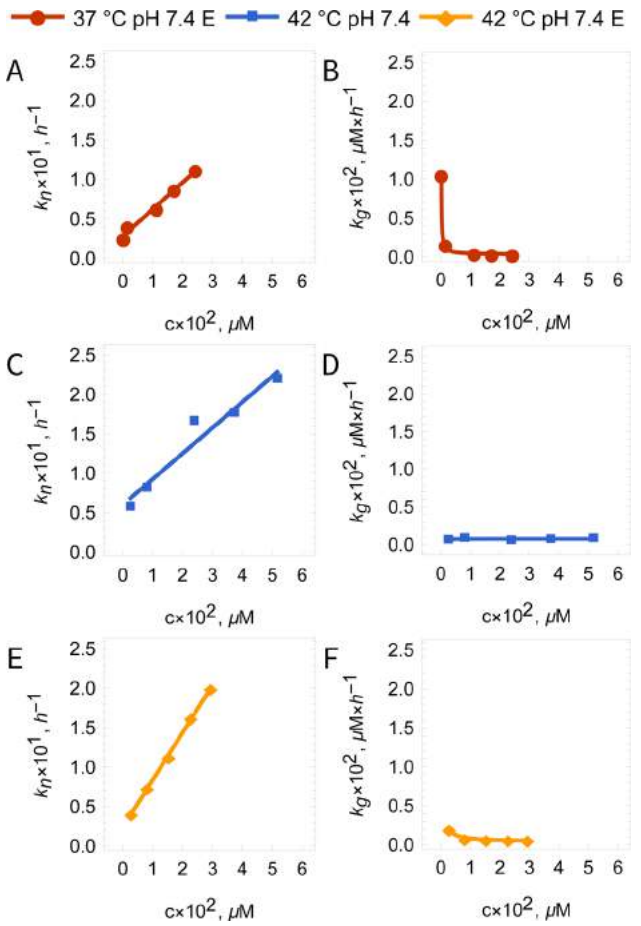

Figure 2. Kinetic rate coefficients for S100A9 amyloid formation calculated according to the F-W model and plotted versus the concentrations of S100A9 amyloids. Nucleation rate coefficients k_n (h^{-1}) are shown in the left column, and growth coefficients k_g ($\mu M \times h^{-1}$) in the right column. The color coding is as in Figure 1A–C. Points correspond to the calculated values of coefficients for each amyloid kinetic curve, and lines correspond to fitting as described in Methods.

used in our experiments as they are both far below protein thermal unfolding temperatures (Figure S1). S100A9 consists of two EF-hand motifs and the lack of calcium ligands destabilizes the calcium-binding loops, promoting misfolding in these most amyloid-prone regions.[15,20] However, apart from the misfolded polypeptide chain, its remaining α-helical conformation cannot be easily packed into cross-β-sheet within amyloid fibril and can hamper fibril growth, as reflected in low growth rate constants k_g and short segments of S100A9 fibrils discussed further (Figure 3).

All samples of S100A9 amyloid fibrils were imaged by atomic force microscopy (AFM) as shown in the representative image in Figure 3A. Fibrillar heights were measured from the AFM cross sections, and the distribution of average fibril heights calculated by bootstrap technique is presented in Figure 3B, inset. S100A9 fibrils are characterized by ca. 3.9 nm average height, which is typical for amyloid fibrils.[7,15] The S100A9 amyloid fibrils do not exceed 200–400 nm in length; i.e., they do not grow up to micrometers as was observed for typical amyloidogenic polypeptides such as Aβ peptide or α-synuclein.[7,22]

By using the image analysis techniques (see Methods), we have derived the quantitative distribution of fibrillar lengths

DOI: 10.1021/acschemneuro.7b00251
ACS Chem. Neurosci. 2017, 8, 2152–2158

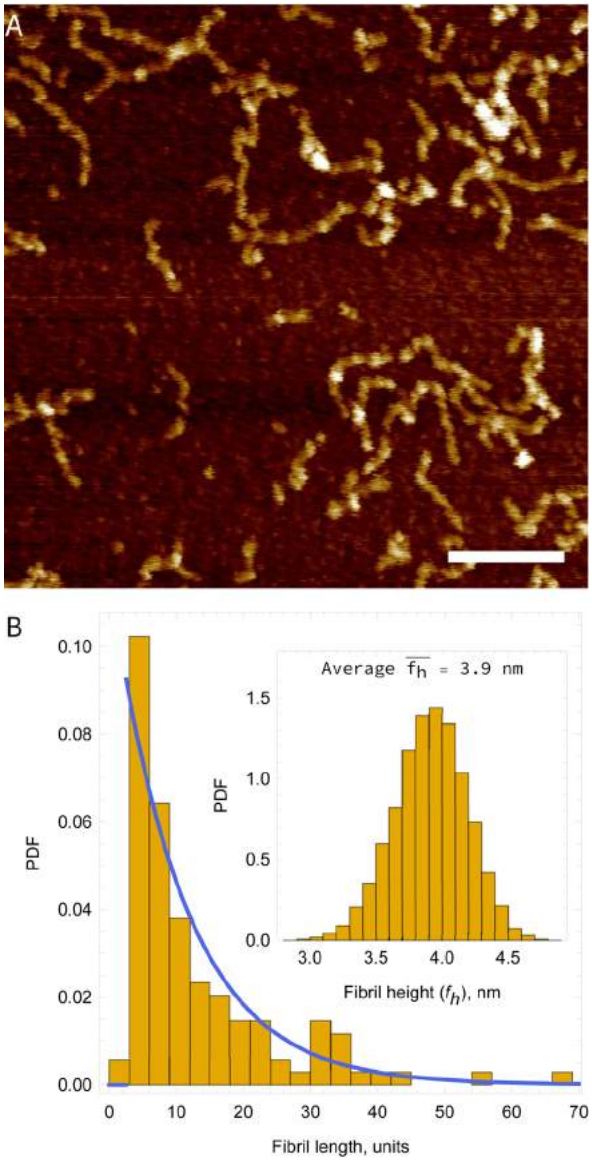

Figure 3. (A) AFM imaging of S100A9 amyloid fibrils assembled during 24 h in PBS, 42 °C, pH 7.4, 238 μM initial S100A9 concentration (the corresponding kinetic curve is marked by an asterisk (*) in Figure 1B). Scale bar equals 200 nm. (B) Equilibrium distribution of S100A9 fibrillar lengths measured by AFM in the above sample. Probability density for corresponding fibril lengths is plotted along *y*-axis, and fibril lengths in units (protein molecules) along the *x*-axis. Line represents fitting of the data set by exponential distribution; the goodness of fit was tested by Kolmogorov–Smirnov criterion.[24] The distribution of average fibril heights measured from the AFM cross sections and calculated by bootstrap analysis is shown in the inset. Probability density for corresponding fibril heights is plotted along *y*-axis, and fibril heights f_h along the *x*-axis.

expressed in number of units or individual molecules assembled into fibrils (Figure 3B). In general, the equilibrium distribution of fibrillar lengths depends on the rates of growth and dissociation as well as on the contribution of some additional processes such as fragmentation or secondary nucleation pathways.[5,23] Therefore, the analysis of S100A9 fibril length distribution provided us an independent approach to evaluate as whether there are contributions of these processes to S100A9 amyloid formation and to compare these with above kinetic experiments. We observed a very good agreement between the experimental and reference exponential distributions of fibrillar lengths described by the Beker–Döring model (eq 7),[23] in which the goodness of the fit was examined by the statistical Kolmogorov–Smirnov test.[24] This indicates that S100A9 amyloid formation indeed proceeds without the contribution of fragmentation and secondary nucleation mechanisms and further confirms the prevalence the F-W two-step nucleation–autocatalytic mechanisms.[5]

The parameter λ, as derived from fitting the fibrillar length distribution shown in Figure 3B by using eq 7, appeared to be equal 0.03; while the ratio of growth and dissociation constants derived from eq 8 equals 0.13. This indicates that the dissociation contribution does not exceed 13% and the S100A9 amyloid formation under pH 7.4 conditions proceeds according to the F-W model.

Fourier transform infrared (FTIR) spectra of native S100A9 and its amyloids formed after 24 h incubation under pH 7.4, 42 °C are shown in Figure 4. FTIR spectrum of native S100A9

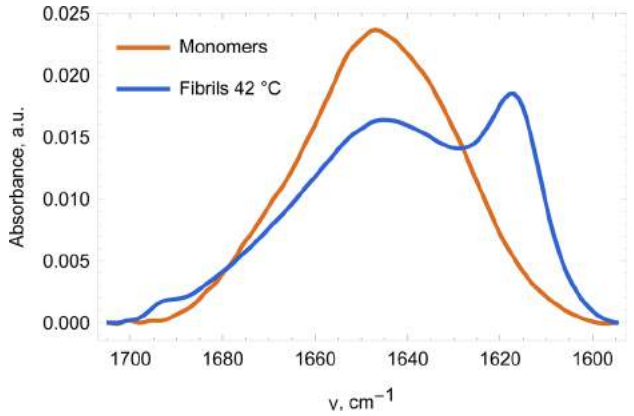

Figure 4. FTIR spectra of S100A9 in the native (orange) and amyloid (blue) conformations corresponding to the kinetic curve marked by an asterisk (*) in Figure 1B and measured in D_2O at room temperature. Arbitrary absorbance units are plotted along the *y*-axis.

displays a broad band in the amide I region with maximum at ca. 1645 cm^{-1}. This strong band originates from four major α-helices in its two EF-hands.[20,25] The band is slightly asymmetrical, reflecting the contributions from turns and flexible C-terminus at ca. 1675 cm^{-1}.

By contrast, the FTIR spectrum of S100A9 amyloid conformation is characterized by a new strong band with maximum at 1615 cm^{-1} and minor band with maximum at 1690 cm^{-1}, demonstrating unequivocally β-sheet formation.[25] The FTIR absorbance in the very broad band with a maximum at ca. 1645 cm^{-1}, reflecting the contribution of α-helices and turns, was significantly reduced compared to the spectrum of native S100A9. The fibrillar sample was centrifuged and resuspended a few times to remove the native protein, however, its contribution to the resulting FTIR spectrum cannot be excluded. This band may also originate from the α-helical and unstructured regions present in native S100A9[20] and preserved within its fibrils. Since we have shown that the nucleation event arises most likely within a single S100A9 molecule, involving part of its structure into β-sheet formation, the residual α-helical and unstructured regions may constitute the fibrillar interface. The presence of such interface within S100A9 fibrils may hinder their growth, which is consistent with the low growth rate and rather short fibrillar length.

DOI: 10.1021/acschemneuro.7b00251
ACS Chem. Neurosci. 2017, 8, 2152–2158

The summary of our observations is shown schematically in Figure 5. Native S100A9 molecules are depicted as white

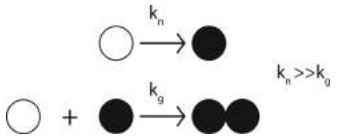

Figure 5. Schematic presentation of S100A9 amyloid assembly according to the F-W nucleation–autocatalysis model. White circle represents the native protein molecule, and black circle the amyloid converted protein. $k_n \gg k_g$.

circles, and misfolded or amyloid converted molecules as black ones. Their molecular conversion, equivalent to the "nucleation" step in the F-W model, dominates over the amyloid growth ($k_n \gg k_g$), where the latter is a rate limiting step in S100A9 amyloid formation.

Thus, the F-W two-step generic model of nucleation followed by autocatalytic self-assembly provides a good analytical description of the kinetics of S100A9 amyloid formation under variety of its concentrations at pH 7.4 and at 37 or 42 °C. The model is minimalistic and does not require any further assumptions or constraints for both processes, considering them as pseudoelementary reactions. By contrast, other available models describing the amyloid assembly process[2,21] did not provide good fits for the S100A9 amyloid kinetics under these conditions, indicating that they are not compatible with the underlying mechanisms of this process. Indeed, the S100A9 kinetics of amyloid assembly did not display the lag-phase, corresponding to protein oligomerization into nuclei, which would be consistent with the model of nucleated-dependent polymerization.[26] The results derived from the F-W model imply that "nucleation" or initial β-sheet conversion may spontaneously take place within individual S100A9 molecules and this process occurs at a higher rate than the subsequent fibrillar growth. The fibrillar growth is described as an autocatalytic process, which takes place if the misfolded "nucleating" conformation persists on a macroscopic time scale. The fact that S100A9 fibrils are characterized by rather short lengths is also consistent with the low growth rate derived from the F-W model. Moreover, the analysis of fibrillar length distribution by using the Bekker–Döring model confirms independently that such distribution is determined by slow fibril growth and there is no fragmentation or secondary pathways, which would also decrease fibrillar length. This emphasizes again that the experimental kinetic data could not be quantified and fitted by using the model of nucleated polymerization with secondary pathways.[2]

Since S100A9 is involved in numerous inflammatory ailments,[7−15] these can lead to significant rise in its concentrations in various organs and tissues to the levels exceeding the concentration of available calcium. If S100A9 conformation is destabilized by calcium dissociation, acidification (Figure S1), commonly occurring upon inflammations and lowering calcium affinity, or other oxidative stress conditions,[10,13,19] these can trigger its spontaneous amyloid formation. S100A9 amyloids can be highly damaging to the tissues as they were shown to be highly toxic to neuronal cells, exceeding the cytotoxicity of Aβ amyloids.[7] They can also accumulate to large quantities in the human brain tissues in Alzheimer's disease or in the aging prostate.[7,15] Our findings presented here indicate that the stabilization of S100A9 structure and inhibition of its misfolding may be explored as amyloid preventing step with therapeutic potential. The application of the F-W model demonstrated a very good description of S100A9 amyloid self-assembly and provided valuable insights into the mechanisms underlying this process. We suggest that this model can be applied to analysis of amyloid aggregation of a wide range of other proteins and peptide under variety of environmental conditions.

METHODS

Protein. S100A9 was expressed in *E. coli* and purified as described previously.[19] Its concentration was measured by using ε_{280} = 0.53 $(\text{mg/mL})^{-1}$ cm^{-1}.

ThT Fluorescence Assay. Measurement of the fluorescence of ThT dye provides a mean of quantitating amyloid since it binds specifically to cross-β-sheet containing structures.[27] It was performed by adding 20 μM ThT to S100A9 solutions kept on ice and pipetted into 96-well plates. The plates were immediately sealed with transparent plastic cover, transferred into a Tecan F200 PRO plate reader, and incubated at preset temperatures without agitation. Corresponding filters were used for ThT emission at 490 nm and excitation at 450 nm, respectively. ThT signals were recoded each 10 min from the bottom of the plate. In control experiments ThT emission was recorded also from the top of the plate, giving similar values. The kinetics were repeated three times using three wells in each repeat for each protein concentration.

Amyloid Formation. To produce amyloids, S100A9 samples were incubated in phosphate buffer saline (PBS), pH 7.4, at 37 or 42 °C. S100A9 solutions (10 mg/mL) were initially centrifuged at 11 000*g* in a cold room at 5 °C for 10 min, and the supernatants were passed through 0.22 μm filters to remove potential amyloid seeds.

The concentrations of S100A9 amyloids after incubation were determined by subjecting the incubated solution to centrifugation at 11 000*g* for 30 min in a cold room at 5 °C, measuring protein concentrations in the supernatants in defined volumes, and subtracting these quantities from the initial protein concentrations. To determine the experimental error, the amyloid concentrations were measured three times. In control experiments, the amyloid pellet was separated in a Beckman Coulter Optima L-90K ultracentrifuge at 417 200*g*, which confirmed the above measurements. The errors in determining the half-times of amyloid formation were calculated from three repeats of corresponding kinetic curves for each S100A9 concentration.

Kinetic Data Analysis. All kinetic curves of S100A9 amyloid formation were well fitted by using the F-W two-step model of nucleation and followed autocatalytic growth:[5]

$$A \xrightarrow{k_n} B \tag{1a}$$

$$A + B \xrightarrow{k_g} 2B \tag{1b}$$

In the first step (eq 1a), native protein A undergoes conversion into misfolded or "active" form B with the rate constant k_n, and then in the second step (eq 1b) the "active" protein B serves as an autocatalyst interacting with remaining native protein A and inducing the amyloid growth with the rate constant k_g. It is important to note that k_g in this scheme is an apparent growth rate constant, taking into account the effects of both growth (k_g*) and dissociation (k_d*) processes occurring simultaneously, and therefore, the steps in the F-W model are called pseudoelementary reactions. The protein concentration A was determined prior to amyloid conversion by measuring optical density of S100A9 solution at 280 nm. The concentration of converted protein B was determined by pelleting amyloid content from solution after the completion of amyloid incubation as described in the above section.

Boundary value problem for this model is presented by following equations, including (a) differential equation for A to B conversion, (b) boundary condition for native species A prior amyloid incubation (A_0), and (c) mass action law for the amyloid growth:

DOI: 10.1021/acschemneuro.7b00251
ACS Chem. Neurosci. 2017, 8, 2152−2158

$$\begin{cases} -\frac{d[A]}{dt} = \frac{d[B]}{dt} = k_n[A] + k_g[A](A_0 - [A]), \\ [A]_{t=0} = A_0 \\ [B] = A_0 - [A] \end{cases} \quad (2)$$

The exact solution of the scheme (eq 2) for the time dependences of amyloid conversion into B conformation is presented below (eq 3) and was used to fit all experimental kinetic data sets:

$$[B](t) = \frac{k_n A_0 (e^{k_n t + k_g A_0 t} - 1)}{k_n e^{k_n t + k_g A_0 t} + k_g A_0} \quad (3)$$

The experimental half-time values (t_{50}) of the amyloid formation kinetics depending on the concentrations of converted protein B were fitted by using eq 4:

$$t_{50} = \frac{\ln\left(\frac{2k_n + k_g A_0}{k_n}\right)}{k_n + k_g A_0} \quad (4)$$

The solutions of both eqs 3 and 4 validate independently the F-W model for describing the S100A9 amyloid kinetics.

Since within the F-W model we consider the amyloid nucleation and growth processes separately, we used the nucleation rate values determined as $k_n[A]$ to estimate the critical nucleus size (n^*) according to the following equation:[28]

$$n^* = \frac{d(\ln k_n[A])}{d(\ln[A])} - 1 \quad (5)$$

Here the nucleation rates were plotted versus the amyloid concentrations, both presented in logarithmic scales, and then the critical nucleus size n^* was determined from the slope of this plot.

AFM Imaging. AFM imaging was carried out by using a BioScope Catalyst atomic force microscope (Bruker) in peak force tapping mode in air. Resolution was set at 512 × 512 pixels, scan size was 1 μm, and scan rate was 1.0 Hz. Peak force set point and gain were controlled automatically. Bruker ScanAsyst-Air cantilevers were used in all measurements. Amyloid samples (10 μL) were deposited on the surface of freshly cleaved mica (Ted Pella) for 15 min, washed three times with 100 μL deionized water, and dried at room temperature.

Fibril Length Distribution Analysis. Fibrillar lengths within the randomly selected AFM imaging fields (five fields of 1 × 1 μm^2 size each) were determined by using image analysis technique in a Wolfram Mathematica 11 analysis package. The *LocalAdaptiveBinarize* and *MorphologicalComponentMeasurements* functions were used to recognize fibrils and measure their dimensions from the processed and digitized AFM images. The quality of amyloid fibril recognition was examined by assigning random color to each recognized fibrillar object and by comparison with their original AFM image.

The length of S100A9 fibrils was represented by the number of units of amyloid assembly (N) and each unit corresponded to S100A9 monomer. The volume of individual fibril was modeled by a cylinder, in which the diameter corresponded to fibrillar height measured in AFM cross-section f_h and the length to fibrillar length l_f. The molecular volume of S100A9 monomer was calculated by using its hydrodynamic radius R_h = 1.55 nm.[7] Then the number of units in amyloid fibrils was estimated according to the equation:

$$N = \frac{l_f \pi \frac{f_h^2}{4}}{\frac{4}{3}\pi R_h^3} \quad (6)$$

The equilibrium distribution of fibrillar lengths was fitted by exponential distribution according to the Becker–Döring model, in which the fibrillar length is represented by linear addition of protein monomeric units and governed by growth and dissociation reactions.[23]

Probability density function (PDF) of exponential distribution is defined by the following equation, where λ is a distribution parameter:

$$PDF(x) = \lambda e^{-\lambda x} \quad (7)$$

By using the Becker–Döring growth-dissociation model, we can estimate the dissociation rate k_d^* from the exponential fibril size distribution by the following equation:[23]

$$\frac{k_d^*}{k_g^*} = [B](e^{-\lambda} + e^{\lambda} - 2) \quad (8)$$

The goodness of the fit of the experimental distribution of fibrillar length by exponential distribution (eq 7) was assessed by the Kolmogorov–Smirnov test.[24] The "distance" between experimental and reference exponential distributions was equal to 0.08 ≪ 1 and the p-value was 0.44 ≫ 0.05, indicating the closeness of these two distributions. The distribution of average fibrillar heights was calculated by using bootstrap technique.[29]

FTIR Spectroscopy. FTIR spectra were recorded using a Bruker Vertex 80v spectrometer equipped with mercury cadmium telluride (MCT) detector. CaF_2 transmission windows and 50 μm Teflon spacers were used. Spectra were recorded at room temperature. Here, 256 interferograms of 2 cm^{-1} resolution were averaged to increase a signal-to-noise ratio. The spectra of D_2O and air were subtracted from the sample spectrum. Linear baseline was applied within the spectral interval of 1705–1595 cm^{-1}, and each spectrum was normalized to the same area of the amide I/I′ band. Data processing was performed by using GRAMS software. Spectrum of native S100A9 was recoded immediately after dissolving 5 mg of protein in D_2O. S100A9 amyloids incubated in 1 mL of PBS at 42 °C for 24 h were pelleted by centrifugation at 15 000g for 30 min and resuspended in D_2O; this procedure was repeated three times to minimize H_2O content. After resuspension, the sample was sonicated for 1 min by using a Bandelin Sonopuls 3100 ultrasonic homogenizer equipped with a MS73 tip.

■ ASSOCIATED CONTENT

Supporting Information

The Supporting Information is available free of charge on the ACS Publications website at DOI: 10.1021/acschemneuro.7b00251.

Method and figure on the thermal unfolding of S100A9 in the presence of various concentrations of $CaCl_2$ (0–30 mM) and under the range of pH from 4 to 10 (PDF)

■ AUTHOR INFORMATION

Corresponding Author

*E-mail: ludmilla.morozova-roche@umu.se.

ORCID

Ludmilla A. Morozova-Roche: 0000-0001-5886-2023

Author Contributions

I.A.I. and D.S. made equal contributions. D.S and M.N.N. performed the experiments. I.A.I. performed calculation and data analysis. V.S. and L.A.M.-R. designed the project. I.A.I. and L.A.M.-R. prepared the manuscript.

Funding

This study was funded by the ALF Västerbotten Läns Landsting (ALFVLL-369861 to L.A.M.-R.), Swedish Medical Research Council (2014-3241 to L.A.M.-R.), FP-7 Marie Curie Action "Nano-Guard" (269138 to I.A.I. and L.A.M.-R.), Insamlingsstiftelsen (FS 2.1.12-1605-14 to L.A.M.-R.), Biochemical Imaging Platform, Umeå University (to L.A.M.-R.), FP-7 Marie Curie Career Integration Grant (293476 to V.S.), and 2016 Erasmus+ program (to D.S.)

Notes

The authors declare no competing financial interest.

DOI: 10.1021/acschemneuro.7b00251
ACS Chem. Neurosci. 2017, 8, 2152–2158

■ ABBREVIATIONS

AFM, atomic force microscopy; ANS, 8-anilino-1-naphthalenesulfonate; F-W, Finke−Watzky; FTIR, Fourier transform infrared; ThT, thioflavin T

■ REFERENCES

(1) Gillam, J. E., and MacPhee, C. E. (2013) Modelling Amyloid Fibril Formation Kinetics: Mechanisms of Nucleation and Growth. *J. Phys.: Condens. Matter 25*, 373101.

(2) Cohen, S. I. A., Vendruscolo, M., Welland, M. E., Dobson, C. M., Terentjev, E. M., and Knowles, T. P. J. (2011) Nucleated Polymerization with Secondary Pathways. I. Time Evolution of the Principal Moments. *J. Chem. Phys. 135*, 065105.

(3) Cohen, S. I. A., Vendruscolo, M., Dobson, C. M., and Knowles, T. P. J. (2011) Nucleated Polymerization with Secondary Pathways. II. Determination of Self-Consistent Solutions to Growth Processes Described by Non-Linear Master Equations. *J. Chem. Phys. 135*, 065106.

(4) Cohen, S. I. A., Vendruscolo, M., Dobson, C. M., and Knowles, T. P. J. (2011) Nucleated Polymerization with Secondary Pathways. IiI. Equilibrium Behavior and Oligomer Populations. *J. Chem. Phys. 135*, 065107.

(5) Watzky, M. A., and Finke, R. G. (1997) Transition Metal Nanocluster Formation Kinetic and Mechanistic Studies. A New Mechanism When Hydrogen Is the Reductant: Slow, Continuous Nucleation and Fast Autocatalytic Surface Growth. *J. Am. Chem. Soc. 119*, 10382−10400.

(6) Morris, A. M., Watzky, M. A., Agar, J. N., and Finke, R. G. (2008) Fitting Neurological Protein Aggregation Kinetic Data via a 2-Step, Minimal/"Ockham's Razor" Model: The Finke−Watzky Mechanism of Nucleation Followed by Autocatalytic Surface Growth. *Biochemistry 47*, 2413−2427.

(7) Wang, C., Klechikov, A. G., Gharibyan, A. L., Wärmländer, S. K. T. S., Jarvet, J., Zhao, L., Jia, X., Shankar, S. K., Olofsson, A., Brännström, T., Mu, Y., Gräslund, A., and Morozova-Roche, L. A. (2014) The Role of Pro-Inflammatory S100A9 in Alzheimer's Disease Amyloid-Neuroinflammatory Cascade. *Acta Neuropathol. 127*, 507−522.

(8) Shepherd, C. E., Goyette, J., Utter, V., Rahimi, F., Yang, Z., Geczy, C. L., and Halliday, G. M. (2006) Inflammatory S100A9 and S100A12 Proteins in Alzheimer's Disease. *Neurobiol. Aging 27*, 1554−1563.

(9) Engel, S., Schluesener, H., Mittelbronn, M., Seid, K., Adjodah, D., Wehner, H. D., and Meyermann, R. (2000) Dynamics of Microglial Activation After Human Traumatic Brain Injury are Revealed by Delayed Expression of Macrophage-Related Proteins MRP8 and MRP14. *Acta Neuropathol. 100*, 313−322.

(10) Postler, E., Lehr, A., Schluesener, H., and Meyermann, R. (1997) Expression of the S-100 Proteins MRP-8 and -14 in Ischemic Brain Lesions. *Glia 19*, 27−34.

(11) Schluesener, H. J., Kremsner, P. G., and Meyermann, R. (1998) Widespread Expression of MRP8 and MRP14 in Human Cerebral Malaria by Microglial Cells. *Acta Neuropathol. 96*, 575−580.

(12) Ma, L. P., Haugen, E., Ikemoto, M., Fujita, M., Terasaki, F., and Fu, M. (2012) S100A8/A9 Complex as a New Biomarker in Prediction of Mortality in Elderly Patients with Severe Heart Failure. *Int. J. Cardiol. 155*, 26−32.

(13) Nagareddy, P. R., Murphy, A. J., Stirzaker, R. A., Hu, Y., Yu, S., Miller, R. G., Ramkhelawon, B., Distel, E., Westerterp, M., Huang, L. S., Schmidt, A. M., Orchard, T. J., Fisher, E. A., Tall, A. R., and Goldberg, I. J. (2013) Hyperglycemia Promotes Myelopoiesis and Impairs the Resolution of Atherosclerosis. *Cell Metab. 17*, 695−708.

(14) Swindell, W. R., Johnston, A., Xing, X., Little, A., Robichaud, P., Voorhees, J. J., Fisher, G., and Gudjonsson, J. E. (2013) Robust Shifts in S100A9 Expression with Aging: a Novel Mechanism for Chronic Inflammation. *Sci. Rep. 3*, 1215.

(15) Yanamandra, K., Alexeyev, O., Zamotin, V., Srivastava, V., Shchukarev, A., Brorsson, A.-C., Tartaglia, G. G., Vogl, T., Kayed, R., Wingsle, G., Olsson, J., Dobson, C. M., Bergh, A., Elgh, F., and Morozova-Roche, L. A. (2009) Amyloid Formation by the Pro-Inflammatory S100A8/A9 Proteins in the Ageing Prostate. *PLoS One 4*, e5562.

(16) Eremenko, E., Ben-Zvi, A., Morozova-Roche, L. A., and Raveh, D. (2013) Aggregation of Human S100A8 and S100A9 Amyloidogenic Proteins Perturbs Proteostasis in a Yeast Model. *PLoS One 8*, e58218.

(17) Horvath, I., Jia, X., Johansson, P., Wang, C., Moskalenko, R., Steinau, A., Forsgren, L., Wagberg, T., Svensson, J., Zetterberg, H., and Morozova-Roche, L. A. (2016) Pro-inflammatory S100A9 Protein as a Robust Biomarker Differentiating Early Stages of Cognitive Impairment in Alzheimer's Disease. *ACS Chem. Neurosci. 7*, 34−39.

(18) Ha, T. Y., Chang, K. A., Kim, J., Kim, H. S., Kim, S., Chong, Y. H., and Suh, Y. H. (2010) S100A9 Knockdown Decreases the Memory Impairment and the Neuropathology in Tg2576 Mice, AD Animal Model. *PLoS One 5*, e8840.

(19) Vogl, T., Leukert, N., Barczyk, K., Strupat, K., and Roth, J. (2006) Biophysical Characterization of S100A8 and S100A9 in the Absence and Presence of Bivalent Cations. *Biochim. Biophys. Acta, Mol. Cell Res. 1763*, 1298−1306.

(20) Itou, H., Yao, M., Fujita, I., Watanabe, N., Suzuki, M., Nishihira, J., and Tanaka, I. (2002) The Crystal Structure of Human MRP14 (S100A9), a Ca^{2+}-Dependent Regulator Protein in Inflammatory Process. *J. Mol. Biol. 316*, 265−276.

(21) Oosawa, F., and Kasai, M. (1962) A Theory of Linear and Helical Aggregations of Macromolecules. *J. Mol. Biol. 4*, 10−21.

(22) Yanamandra, K., Gruden, M. A., Casaite, V., Meskys, R., Forsgren, L., and Morozova-Roche, L. A. (2011) α-Synuclein Reactive Antibodies as Diagnostic Biomarkers in Blood Sera of Parkinson's Disease Patients. *PLoS One 6*, e18513.

(23) Prigent, S., Haffaf, H. W., Banks, H. T., Hoffmann, M., Rezaei, H., and Doumic, M. (2014) Size Distribution of Amyloid Fibrils. Mathematical Models and Experimental Data. *Int. J. Pure Appl. Math 93*, 845−878.

(24) Stephens, M. A. (1974) EDF Statistics for Goodness of Fit and Some Comparisons. *J. Am. Stat. Assoc. 69*, 730−737.

(25) Barth, A. (2007) Infrared Spectroscopy of Proteins. *Biochim. Biophys. Acta, Bioenerg. 1767*, 1073−1101.

(26) Harper, J. D., and Lansbury, P. T. (1997) Models of Amyloid Seeding in Alzheimer's Disease and Scrapie: Mechanistic Truths and Physiological Consequences of the Time-Dependent Solubility of Amyloid Proteins. *Annu. Rev. Biochem. 66*, 385−407.

(27) Xue, C., Lin, T. Y., Chang, D., and Guo, Z. (2017) Thioflavin T as an Amyloid Dye: Fibril Quantification, Optimal Concentration and Effect on Aggregation. *R. Soc. Open Sci. 4*, 160696.

(28) Kashchiev, D., and Auer, S. (2010) Nucleation of Amyloid Fibrils. *J. Chem. Phys. 132*, 215101.

(29) DiCiccio, T. J., and Efron, B. (1996) Bootstrap Confidence Intervals. *Stat. Sci. 11*, 189−228.

DOI: 10.1021/acschemneuro.7b00251
ACS Chem. Neurosci. 2017, 8, 2152−2158